Additive Manufacturing 48 (2021) 102410

Contents lists available at ScienceDirect

Additive Manufacturing

journal homepage: www.elsevier.com/locate/addma

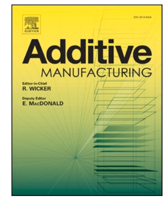

Research Paper

# Design, manufacture and characterization of compact filter assemblies for radiofrequency applications

J.M. Lopez-Villegas *, N. Vidal, A. Salas

*Department of Electronic and Biomedical Engineering, RF Group, University of Barcelona, E-08028 Barcelona, Spain*

ARTICLE INFO

*Keywords:*
Additive manufacturing
3D printing electronics
RF Non-planar circuits
Conical inductor
Low-pass filter

ABSTRACT

This paper presents the use of additive manufacturing in the design and fabrication of a non-planar fully 3D-printed low-pass filter. The process implements stereolithographic 3D printing and copper electroplating to produce the necessary parts and their casing. The filter we produce acts as a demonstrator: we present the possibility of constructing building blocks and combining different elements into a full assembly for system integration. We introduce the "drop-and-screw" concept, which is implemented to mount the parts into a single connectorized assembly without the need for welding. The method we propose may be suitable for building other components by simply changing the building blocks. We pay special attention to the design of the constituent parts of the filter (a 3D conical inductor and a 3D capacitor), exploring new geometries to reduce the size of the final filter prototypes. The results demonstrate the potential of additive manufacturing in the construction of high-performance RF components and assemblies, and we present a modular prototype with a high degree of reconfigurability and multifunctionality.

## 1. Introduction

There is no doubt that additive manufacturing (AM) is a technological revolution [1]. It is not only an innovation, but also an incremental advancement in many aspects with respect to traditional manufacturing methods. AM is having a huge impact in some sectors such as the aerospace, biomedical, automotive, and consumer goods industries [2]. The electronics manufacturing field has also been impacted, although the influence of 3D printing technology is not as pervasive as in other production areas. The current market is relatively small [3] and there are still many opportunities and challenges to address [4,5]. For instance, it would be possible to achieve increased integration and compactness of the electronics. Improvement in designs and performance resulting from the 3D implementation of existing components and circuits would also be possible; and new components and circuit designs that have no planar counterparts could even be introduced. To achieve this, it will be necessary to develop new printing materials, including low-loss dielectrics and high-conductivity metals, as well as the possibility of mixing them. AM has high potential to transform the electronics manufacturing industry [5].

In the specific area of radiofrequency (RF) components and circuits, there is generally not a widespread use of 3D printing. The full potential of directly applying AM to produce RF components has been already pointed out [6–8]. The AM of passive and active components has been a growing focus of research in recent years. Many studies have focused mainly on 2D printing methods, such as inkjet printing or roll-to-roll printing, to produce capacitors, inductors, transistors, antennas, sensors, and RFID tags, among others [6,9,10].

Full-scale 3D printing of electronics is still at an early stage. However, it is worth noting the studies on 3D printing in the production of antennas and electromagnetic (EM) structures [11–15]. Likewise, there are also relevant studies in the literature about the use of 3D printing for implementing RF and microwave components and circuits [6,16–20], including resonators [21], transmission lines [22,23], and even the components of a RF Front-End operating at the 2.45 GHz frequency band [24]. However, only a few of these studies have taken advantage of a fully 3D design to implement RF components and circuits. Some of these methods involve multi-layer implementations, where the vertical dimension is mainly used for level-to-level interconnection. One main challenge is related to the metallization process. Most of the fully 3D designs involve total metallization. When the metallization is partial, the methodology is much more complex and there are fewer examples of this in the literature. Partial metallization can be obtained, for example, by using a mask, by selective laser etching or by selective metallization

* Corresponding author.
*E-mail address:* j.m.lopez_villegas@ub.edu (J.M. Lopez-Villegas).

https://doi.org/10.1016/j.addma.2021.102410
Received 14 June 2021; Received in revised form 1 September 2021; Accepted 13 October 2021
Available online 19 October 2021
2214-8604/© 2021 The Authors. Published by Elsevier B.V. This is an open access article under the CC BY-NC-ND license (http://creativecommons.org/licenses/by-nc-nd/4.0/).

[25,26]. These procedures are quite simple for 2D structures, but more complex for fully 3D devices.

The AM of RF components and circuits can be used to escape from planarity and, in some cases, improve performance as well as increase the compactness of electronic devices. It gives greater freedom in designing and reduces restrictions in manufacturing. Therefore, AM can not only be used to build fully 3D components, but it can also provide a great opportunity for assembly [27,28]. In this work, we present a compact fully 3D printed low-pass filter (LPF), intended to operate in the RF frequency band. The filter acts as a demonstrator, presenting the possibility of constructing building blocks and combining different elements into a full assembly for whole system integration. We also introduce the drop-and-screw concept, which is used to mount the parts into a single connectorized assembly without the need for welding. The proposed method may be suitable to reconfigure the filter by simply changing the building blocks.

Filters are basic building blocks in the design of electronic circuits. In the RF and microwave (μW) frequency bands, the design of filters requires the use of high-performance passive components. This represents a particular challenge in the case of inductors. Inductor losses, either ohmic or magnetically induced, are the main drawback that limits the quality factor (Q) [29,30]. The self-resonant frequency (SRF) sets the upper limit of the frequency at which the component can function properly. The Q of the inductor directly determines the insertion losses of the filter it belongs to, while its SRF directly determines the operating bandwidth of the filter. In the search for better inductor designs, conical geometry has attracted great interest. Conical inductors have a wider working bandwidth than inductors with other topologies [31–33]. The usual method to manufacture these components is to wind copper wire into the form of a cone. The resulting structure constitutes a non-planar lumped device. Some examples of conical inductors designed using multilayered technologies can be found in the literature [34]. However, a fully 3D implementation is required to take full advantage of the potential of these components. It is for this reason that 3D printing technology is highly suited to the manufacture of high-quality conical inductors [20].

Regarding the capacitor design, some 3D implementations of metal-insulator-metal (MIM) capacitors in silicon substrates have been reported. As stand-alone devices embedded in the substrate or combined with through-substrate vias (TSVs), these capacitors can result in a significant increase in the capacitance density when compared with trench or stacked capacitors [35–37].

In this work, we pay special attention to the design of a 3D conical inductor and a 3D capacitor, exploring new geometries to compact the final filter assembly as much as possible, while maintaining the broadband operation of the filter. We also focus our efforts on the design of the filter packaging. Custom cases will be designed, and 3D printed to arrange the different filter prototypes. The drop-and-screw concept will then be used for the final assembly. The whole set presents a modular prototype suitable for exchanging components. The aim is to provide a high degree of reconfigurability and multifunctionality. The set should be customizable, providing flexibility from design to specification.

## 2. Methods and modelling

In this section, we describe the process of the design and optimization of the 3D conical inductors and the 3D capacitors used in the filter prototypes. We report EM simulations using the finite element method (FEM) to optimize the EM behavior of the passive components, and to tune the inductance and capacitance values to those required to implement a third-order T-type Butterworth LPF [38]. The simulation data for the passive components are combined in a circuital simulator to obtain a preliminary assessment of the performance of the LPF and to compare this with the response of an ideal filter. To design the LPF prototypes, we chose an LC-ladder topology. Table 1 summarizes the filter specifications. According to the Butterworth formulae [38], the target cut- off frequency of 250 MHz can be achieved using inductance and capacitance values of 31.8 nH and 25.5 pF, respectively. In the following subsections, we describe the different steps in the design and fabrication process of the components and packaging.

**Table 1**
Filter characteristics.

| Topology | LC-ladder T-section third order 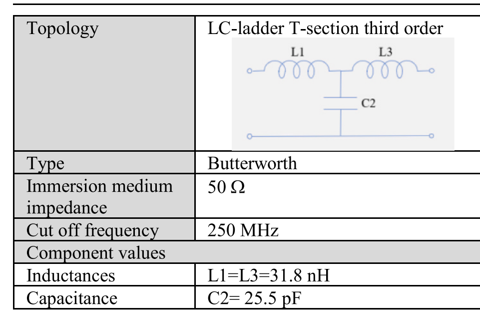  |
|---|---|
| Type | Butterworth |
| Immersion medium impedance | 50 Ω |
| Cut off frequency | 250 MHz |
| Component values | |
| Inductances | L1=L3=31.8 nH |
| Capacitance | C2= 25.5 pF |

### 2.1. Inductors

The design, optimization, and the EM analysis, of the conical inductors, were all carried out using EMPro [39]. The design process began with the definition of the geometry and constituent materials of the conical inductor. The base geometry is a truncated cone, for which we made from a photopolymer used in stereolithographic 3D printing. We performed EM characterization of the material using the resonant-cavity and the coaxial-line methods [40]. The metal parts were defined on the surface of the base geometry. A metal spiral rounds around the truncated cone and connects two plates at the top and bottom of the component. The EM properties of the metal used are those of bulk copper. Fig. 1 shows an example of the resulting CAD model of the 3D inductor together with the main design parameters. To speed up the optimization algorithm, only two geometrical parameters were varied to reach the required quasi-static inductance: the cone angle and the number of turns in the spiral. The other parameters were fixed (Fig. 1).

The target value of the inductances L1 = L3 = 31.8 nH, can be obtained using different combinations of $\alpha$ and $N$. This fact is illustrated in Fig. 2. In the figure, the equivalent inductance of a conical inductor geometry, derived from FEM simulations, is plotted as a function of the cone angle for three values of the number of turns in the spiral. The target value of 31.8 nH is also indicated as a horizontal dashed line. The intersections of this line with data curves correspond to actual implementations of the component. For instance, the pairs of $\alpha$ and $N$ equal to: (8.9°, 3), (54°, 2.5) and (133°, 2.3) correspond to inductors with the desired inductance value. Schematic views of the resulting inductor geometries are shown in each case.

Two design objectives should be met at the same time. First, the component must be as compact as possible. Second, the operating bandwidth of the inductor must be as large as possible. When concerned with compactness, we have to consider the overall size of the component, not just its height or the area of its base. Accordingly, to quantify the compactness of the conical inductor implementations, we defined a figure of merit (FOM) as the volume of the smallest sphere that contains the component. Fig. 3, shows the FOM values as a function of $\alpha$ for a set of 19 inductors, that includes the three inductors shown in Fig. 2. In all the cases, for a given value of the cone angle the number of turns $N$ is adjusted so that the inductance is 31.8 nH. It can be observed that the most compact designs correspond to small cone angles (i.e., there is a minimum for $\alpha \approx 20^{\circ}$). Moreover, the FOM shows a notable increase from $\alpha \approx 60^{\circ}$ until planar spiral geometry is reached (i.e., $\alpha = 180^{\circ}$).

Concerning the bandwidth enhancement, measured in terms of the SRF, a previous study concluded that this frequency increase from $\alpha = 0^{\circ}$ (a solenoid inductor) up to $\alpha =$ 50–60°, and remains almost unchanged until $\alpha = 180^{\circ}$ (a planar spiral inductor) [20].

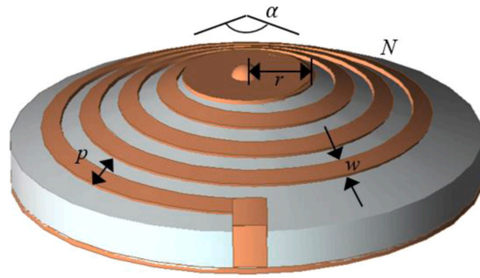


| Geometry | | |
|---|---|---|
| $\alpha$ | cone angle | optimized |
| $r$ | radius of the top circular surface | 3 mm |
| $N$ | number of turns in the spiral | optimized |
| $p$ | pitch between turns | 2 mm |
| $w$ | metal strip with | 1 mm |
| Materials | | |
| metal | conductivity (bulk copper) | $5.8\ 10^7$ S/m |
| dielectric | permittivity | 2.9 |
| | loss tangent | 0.02 |

**Fig. 1.** CAD model of the conical inductor together with the main design parameters.

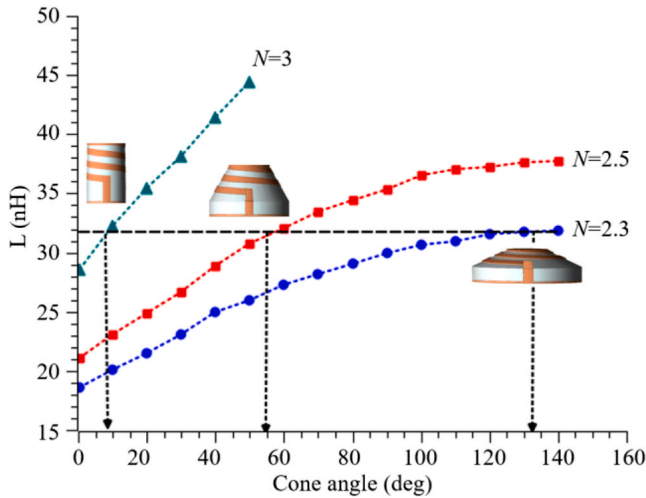


**Fig. 2.** Plot of the equivalent inductance as a function of the cone angle, $\alpha$, for different values of the number of turns, $N$. The horizontal dashed line indicates the target value of 31.8 nH. The inset images correspond to schematic views of possible conical inductor implementations.

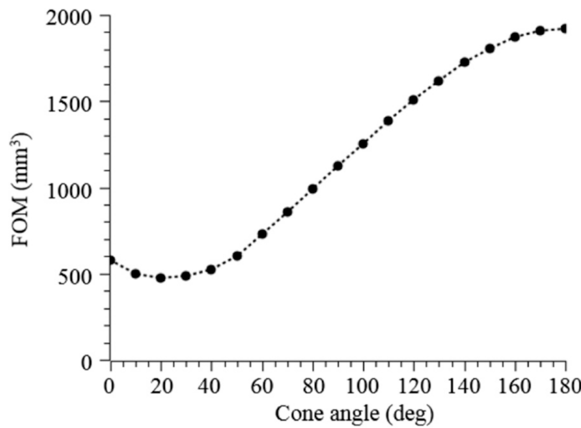


**Fig. 3.** Plot of the compactness FOM as a function of α for a set of inductors. The target inductance value is 31.8 nH.

In accordance with both the foregoing considerations, a trade-off between compactness and bandwidth enhancement would be to select a cone angle between 50° and 60°. In practice, iterative simulations were performed within the defined constrains to reach the required inductance (i.e., 31.8 nH). The best match was achieved with: $N = 2.5$ and $\alpha = 54°$.

### 2.2. Capacitors

The capacitor design starts from a coaxial waveguide segment. The initial model is shown in Fig. 4a. The simplest capacitance geometry is obtained by connecting the outer conductor of the coaxial waveguide to a metal ring that extends perpendicularly, out to a certain radius, $\rho$. The internal conductor is connected to a metal disk, with the same external radius as the ring, and separated by a distance, $d$. The internal dielectric material is the same as that used for the inductor model. The electrical coupling between the ring and the plate produces the final capacitance. To reduce the dimensions of the optimization space, only $\rho$ is varied in the optimization algorithm. The length of the coaxial segment and the distance between the ring and the plate are fixed to the minimum suitable values. These last constrains allow us to achieve the maximum capacitance density. The final model (CM1) shown in Fig. 4b is the result of combining two equal parts.

This simple capacitor model led to quite a compact component geometry if, $\Delta x \approx \rho$. This would be the case when small values of capacitance are required. However, if the required capacitance is large, then $\rho > \Delta x$, and the compactness of the component compared with that of the inductors could be a concern. To avoid this drawback, we proposed a modified more complex capacitor geometry. Using as our starting point the simple geometry, the new version is obtained by bending the edges of the vertical ring and circular plate to form a coaxial structure. Fig. 5 shows the obtained result (CM2). In this case, to obtain the desired capacitance, besides the radius, $\rho$, the length of the edge of the coaxial segment, $\Delta t$, was also introduced into the optimization process.

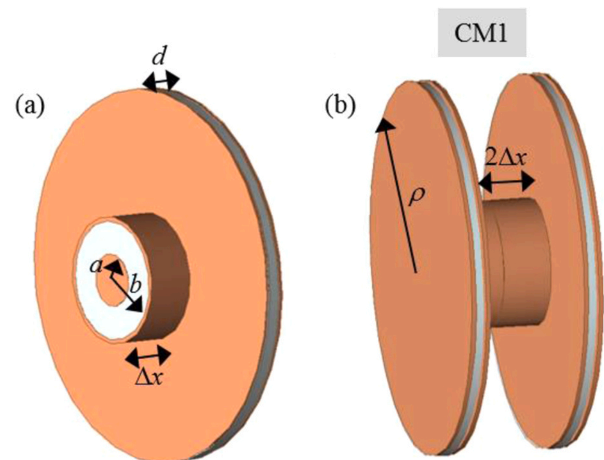


| | | |
|---|---|---|
| $a$ | coaxial waveguide inner radius | 1.25 mm |
| $b$ | coaxial waveguide outer radius | 3 mm |
| $\Delta x$ | coaxial waveguide segment | 2.5 mm |
| $\rho$ | metal ring radius | optimized |
| $d$ | metal ring length | 0.5 mm |
| $2\Delta x$ | coaxial waveguide middle segment | 5 mm |

**Fig. 4.** Capacitor model CM1: half (a) and complete (b) structure.

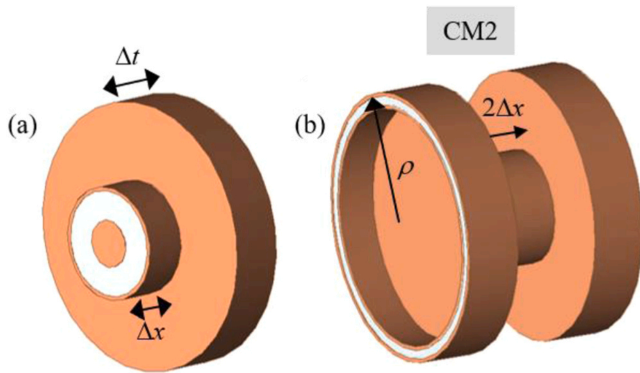


**Fig. 5.** Capacitor model CM2: half (a) and complete (b) structure.

Simulations were performed for the two capacitator models. In the case of CM1, the plate radius, $\rho$, was adjusted to achieve the target capacitance (i.e., 25.5 pF). Iterations were performed and the result was a plate radius of 8.8 mm. In the case of the modified capacitor model CM2, the plate radius, $\rho$, was fixed at 7.0 mm, which left enough space to accommodate the inductors on both sides. Finally, the length of the edge of the coaxial segment, $\Delta t$, was adjusted. The target capacitance was achieved with $\Delta t = 2.2$ mm. We should mention that in both cases (CM1 and CM2), the central coaxial segment introduces a certain capacitance and inductance, which were also taken into consideration in the EM simulations.

### 2.3. Filter: CAD models

The CAD models of the LPF prototypes were constructed by combining two 3D conical inductors with one of the 3D capacitors. The ensembles are shown in Fig. 6. The electrical performance of the LPF1 and LPF2 prototypes was preliminarily evaluated by circuital simulation [41]. The inductors and capacitors were taken as data blocks and the response of the CAD models was calculated. The results were compared with the reference filter response. Fig. 7 shows a comparison of the LPF responses obtained for frequencies up to 2.5 GHz (i.e., ten times the cut-off frequency). It can be observed that the expected responses of the LPF prototypes are almost the same, only at frequencies greater than 1.5 GHz are small differences observed.

In both cases, the expected responses of the LPF models correspond to that of the ideal filter up to 400 MHz. From that point on, an increase in rejection losses is observed. This can be attributed to the resonances of the components. Fig. 7 also shows (blow up) the behaviour near the cut-off frequency.

Both LPF prototypes had expected cut-off frequencies in the range of 247–248 MHz, which corresponds to an error of about 1% with respect to the target value of 250 MHz. Concerning the passband (i.e., up to the cut-off frequency), small insertion losses are observed for both filter prototypes, which are mainly due to the non-zero resistance of the metal parts and the loss tangent of the dielectric material used in the CAD model. It should be noted that the seed is not included in the CAD model, because most of the electrical current passes through the high-conductivity copper layer that is grown on it. Therefore, the effect of seed losses can be ignored in comparison with copper losses. Due to its length, metal losses are particularly important in the metal spiral of the conical inductors. Meanwhile, the dielectric losses are almost independent of the operating frequency and are not expected to make an important contribution to overall losses of the filter prototypes, which are intended to work in the low RF band (i.e., hundreds of MHz).

### 2.4. Additive manufacturing

A detailed description of the manufacturing process of the

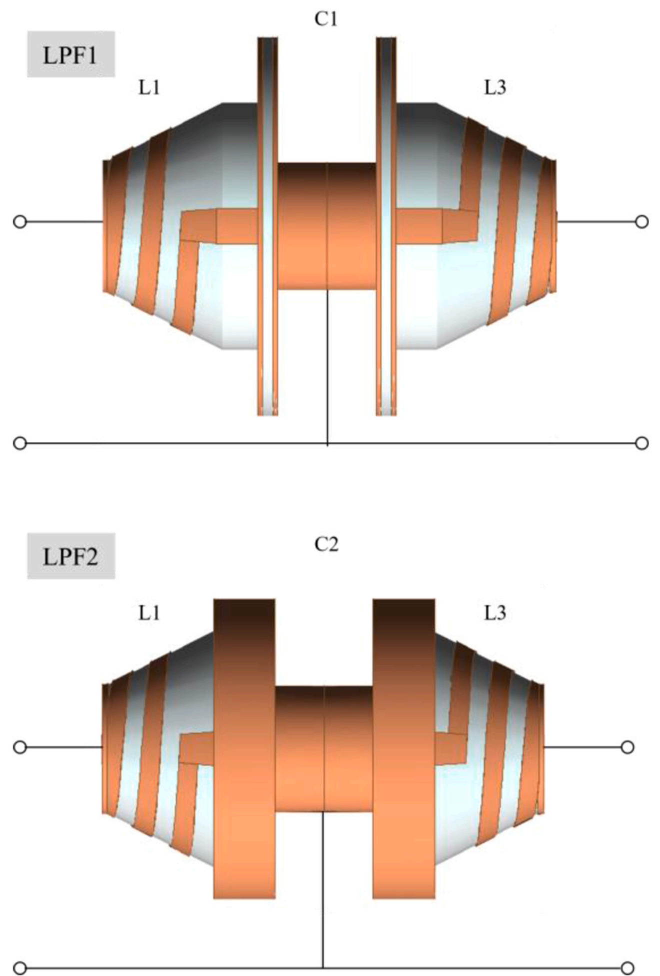


**Fig. 6.** CAD models of the LPF prototypes with the simple LPF1 (top) and the modified LPF2 (bottom) 3D capacitor designs.

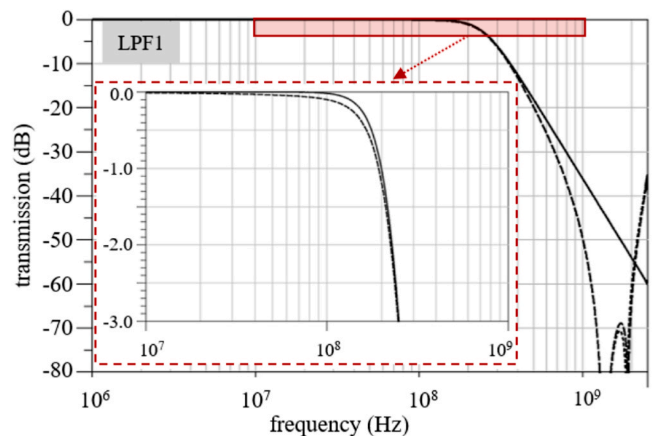


**Fig. 7.** Comparison of the responses of the LPF prototypes with that of the ideal filter. The continuous line corresponds to the ideal filter, the dashed line to the LPF prototype with a simple 3D capacitor (LPF1), and the dotted line to the LPF prototype with a modified 3D capacitor (LPF2).

components can be found in [42]. For the sake of completeness, the main steps are explained in the following subsections.

#### 2.4.1. CAD environment

To fabricate the passive components an initial setup was necessary in

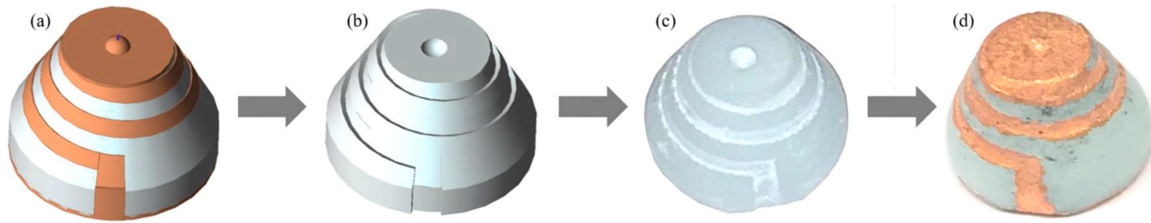


**Fig. 8.** Manufacturing process for the conical inductor: (a) base geometry, (b) structure used to fabricate, (c) structure after 3D printing and, (d) finished part.

the CAD environment. Fig. 8 illustrates the whole manufacturing process. The first step is performed using the Boolean operators available in the CAD environment and consists of subtracting the metal parts from the dielectric body, as shown in Fig. 8a and b. In the case of the inductor, after this procedure we obtained trenches that correspond with the spiral geometry (Fig. 8b). In the case of the capacitor, the procedure generated a spool-like geometry, which is simple or with bent edges, depending on the model. It should be noted that the metal parts are used as a 3D mask to virtually etch the base geometry they sit on. After subtracting the metal parts, we coded the resulting structures and sent them to the 3D printer. We used a high precision stereolithographic printer. Fig. 8c shows the raw structure corresponding to the printed conical inductor.

### 2.4.2. *Copper plating*

The base structures were metallized using electroless copper plating and/or copper electroplating. This procedure requires a conductive seed layer. Previous studies showed that there is no need for a highly conductive seed layer. In fact, the use of conductive filaments based on black carbon as seeds for copper electroplating has been reported [43]. In our case, after some trials, suitable seeding was achieved using a coating based on silver or nickel. In both cases, the seed adhered adequately to the base structure and allowed for correct growth of the copper layer without exfoliation. An initial coating was created by spraying the printed parts all over. This provided a quite uniform seed layer, few microns thick, on the constituent parts, including inside the vias. Then, we manually polished the silver or nickel off the unwanted areas. For the conical inductors, we left the seed in the trenches and on the contact surfaces at both sides of the component. For the capacitor, the seed was only removed from the edges of the plate (CM1) or from both sides (CM2). Finally, the parts where the seed layer remained were metallized using electroless copper plating and/or copper electroplating. In all cases, a copper sulfate electrolyte was used. The final thickness of the copper layer depends on the geometry of the part, the temperature (particularly in the case of electroless plating), the current density (in electroplating) and the processing time. Usually, at room temperature and with a processing time of 1 h, the resulting copper layer is in the range from 20 to 40 μm thick and the conductivity is about $10^7$ S/m. The final conical inductor and capacitors obtained are shown in Fig. 8d and Fig. 9.

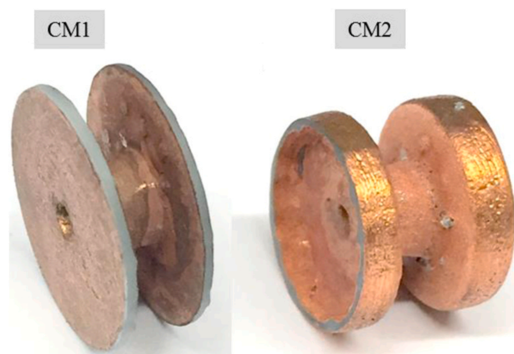


**Fig. 9.** Example of finished parts after copper plating. From left to right: 3D simple conical capacitor, and 3D modified capacitor.

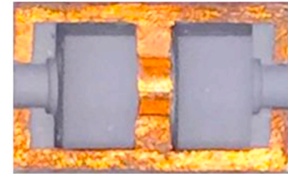

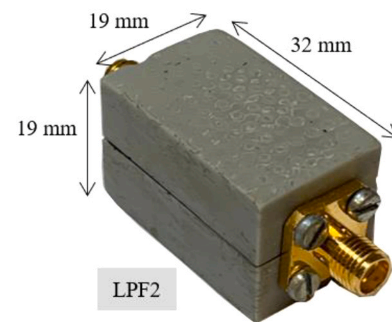


**Fig. 10.** Example of printed custom half (top) and packing case (bottom).

### 2.4.3. *Filter mounting: packaging*

To implement the LPF prototypes, a packing case was designed to house the components. The casing was printed and metallized using the same procedure described in the previous sections. Finally, the optimized inductor and capacitors were aligned inside the casing. It is important to note that the metallized parts of the casing provide grounding and allow input and output via SMA connectors. As an example, the final LPF2 half and full casings are shown in Fig. 10.

## 3. Results and discussion

Considering all the previous steps, all the filter parts were placed and interconnected inside the custom case. We used the drop-and-screw concept. This means that soldering is not required. Electrical contact is achieved thanks to the pressure provided by the connectors. Fig. 11 shows an image of the final arrangements of both LPF prototypes. The final dimensions, without the SMA connectors, are: $23 \times 23 \times 32$ mm$^3$ for the LPF prototype with the simple 3D capacitor design (LPF1); and $19 \times 19 \times 32$ mm$^3$ for the LPF prototype with the modified 3D capacitor design (LPF2).

In order to characterize the LPF prototypes, the S-parameters were measured from 1 MHz to 2.5 GHz, using a vector network analyser. The measured transmission parameter (S21) of the LPF prototypes is shown in Fig. 12. The same figure also includes plots of the ideal Butterworth filter response, together with the results obtained from our circuital simulations. Good agreement can be observed between the experimental data, the circuital simulation, and the ideal filter behaviour. The transmission of both LPF prototypes in the stop band is slightly different from that of the reference filter. For frequencies up to 1.7 GHz, in the case of

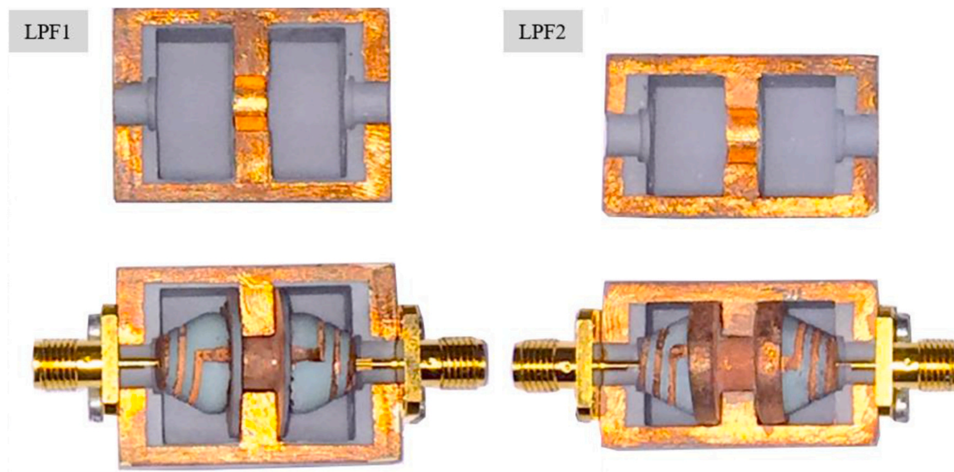


**Fig. 11.** LPF prototypes mounted in the 3D printed custom cases that are ready for testing.

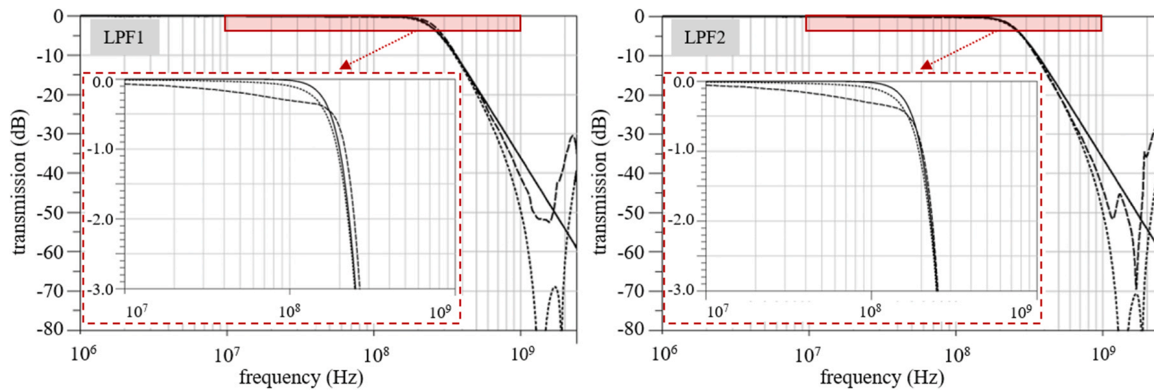


**Fig. 12.** Results for the transmission parameter of the LPF prototypes (dashed line) together with the CAD model circuital simulations (dotted line). The ideal filter response (continuous line) is also included in the plots.

LPF1, and up to 1.8 GHz, in the case of the LPF2, the rejection loss is somewhat larger than that of the ideal filter. Above these frequencies, degradation of the filter responses is observed, in agreement with the expected results obtained from the CAD model simulations.

The figure also shows the transmission parameter from − 3 to 0 dB, for frequencies from 10 MHz to 1 GHz, which allows us to analyse the behaviour of the LPF prototypes in the passband. Looking at the intersection between the curves and the x-axis, we can determine the actual cut-off frequency of the prototypes. For the LPF1 prototype, the cut-off frequency obtained this way is equal to 262 MHz, which means an error of 4.8% on the target value of 250 MHz. In contrast, in the case of the LPF2 prototype the value for the cut-off frequency obtained is equal to 253 MHz; an error of 1.2% on the target value. These discrepancies must be related to the tolerance of the printing process and variability of the EM characteristics related with the printing material.

As shown in Fig. 12, the behavior in the passband, up to the cut-off frequency, is quite similar for both filter prototypes. In both cases, the maximum insertion loss at the low frequency limit is 0.1 dB. The maximum increase in insertion loss compared with the reference filter is 0.30 dB for the LPF1 prototype and 0.32 dB for LPF2, across the whole passband. Our results indicate that the two filter prototypes have very similar performance. According to this, it should be noted that the increase in the compactness of the LPF2 in comparison with LPF1, which is related to the use of the modified 3D capacitor, does not worsen the performance of the filter.

## 4. Conclusions

In this work, we present the design, optimization, production and EM characterization of compact LPF prototypes. Our results demonstrated the potential of AM in the implementation of high-performance RF components and assemblies. A third order T-type Butterworth filter was chosen as the filter topology. The prototypes were designed using 3D conical inductors and 3D capacitors. The conical inductors were designed considering the compactness of the component and the frequency bandwidth enhancement. A figure of merit was proposed to quantify compactness. A trade-off was established between the two requirements, leading to an optimum inductor. Two geometries of 3D capacitors were also considered: a simple spool-like geometry and a modified geometry with bent edges to increase compactness. EM models of two LPF prototypes were constructed by combining two conical inductors and one of the 3D capacitors. As a test of the design process, circuital simulations of the filter CAD models were carried out using FEM data from the optimized components, and the expected behaviour was compared with the reference filter response. Once the design phase was complete, the passive components and the cases for filter packaging were printed and metallized. Two LPF prototypes were mounted, using a drop and screw concept which avoids the need for welding, and then tested. LPF1 incorporated the simple 3D capacitor design; LPF2 the modified 3D capacitor design. The electrical performance of the fabricated LPF prototypes was in good agreement with the expected

frequency response of the filter CAD models, obtained by circuital simulations, and with the response of reference filter.

The results of our EM characterization of the filter prototypes deviate less than 5% from the target design specifications in terms of cut-off frequency and insertion loss. This validates the whole manufacturing process. Finally, it is worth noting that the design of both the filter components and the casings allows for reconfigurability, through changing the inductors and capacitors for other constituent parts from a library of predefined devices; and for multifunctionality, by modifying the topology, to implement high-pass filters instead of low-pass filters for instance.

## Declaration of Competing Interest

The authors declare that they have no known competing financial interests or personal relationships that could have appeared to influence the work reported in this paper.

## Acknowledgment

This work was supported by the Spanish Ministry of Economy and Competitiveness, project TEC2017-83524-R.

## References

[1] The 3-D Printing Revolution, n.d. ⟨https://hbr.org/2015/05/the-3-d-printing-revolution⟩ (Accessed 22 February 2021).
[2] The disruptive nature of 3D printing, 2017.
[3] Printed Electronics Market by Printing Technology, Application, Material, End-Use Industry | COVID-19 Impact Analysis | MarketsandMarketsTM, n.d. ⟨https://www.marketsandmarkets.com/Market-Reports/printed-electronics-market-197.html⟩ (Accessed 22 February 2021).
[4] E. MacDonald, R. Salas, D. Espalin, M. Perez, E. Aguilera, D. Muse, R.B. Wicker, 3D printing for the rapid prototyping of structural electronics, IEEE Access 2 (2014) 234–242, https://doi.org/10.1109/ACCESS.2014.2311810.
[5] A.H. Espera, J.R.C. Dizon, Q. Chen, R.C. Advincula, 3D-printing and advanced manufacturing for electronics, Prog. Addit. Manuf. 4 (2019) 245–267, https://doi.org/10.1007/s40964-019-00077-7.
[6] R. Sorrentino, P. Martin-Iglesias, O.A. Peverini, T.M. Weller, Additive manufacturing of radio-frequency components [scanning the issue], Proc. IEEE 105 (2017) 589–592, https://doi.org/10.1109/jproc.2017.2670298.
[7] E. MacDonald, R. Wicker, Multiprocess 3D printing for increasing component functionality, Science 80 (2016) 353, https://doi.org/10.1126/science.aaf2093.
[8] I.O. Saracho-Pantoja, J.R. Montejo-Garai, J.A. Ruiz-Cruz, J.M. Rebollar, Additive manufacturing of 3D printed microwave passive components, in: Emerg. Microw. Technol. Ind. Agric. Med. Food Process., InTech, 2018, https://doi.org/10.5772/intechopen.74275.
[9] H.W. Tan, T. Tran, C.K. Chua, A review of printed passive electronic components through fully additive manufacturing methods, Virtual Phys. Prototyp. 11 (2016) 271–288, https://doi.org/10.1080/17452759.2016.1217586.
[10] N. Saengchairat, T. Tran, C.K. Chua, A review: additive manufacturing for active electronic components, Virtual Phys. Prototyp. 12 (2017) 31–46, https://doi.org/10.1080/17452759.2016.1253181.
[11] Guest Editorial: Microwave Components and Antennas based on advanced manufacturing techniques, IET Microwaves, Antennas Propag. 11, 2017, pp. 1919–1920. ⟨https://doi.org/10.1049/iet-map.2017.1007⟩.
[12] S.K. Sharma, H. Xin, B.I. Wu, J.C. Vardaxoglou, C.H. Chan, Guest editorial special cluster on three-dimensional printed antennas and electromagnetic structures, IEEE Antennas Wirel. Propag. Lett. 17 (2018) 1998–2002, https://doi.org/10.1109/LAWP.2018.2877472.
[13] D. Helena, A. Ramos, T. Varum, J.N. Matos, Antenna design using modern additive manufacturing technology: a review, IEEE Access 8 (2020) 177064–177083, https://doi.org/10.1109/access.2020.3027383.
[14] R. Colella, F.P. Chietera, F. Montagna, A. Greco, L. Catarinucci, Customizing 3D-printing for electromagnetics to design enhanced RFID antennas, IEEE J. Radio Freq. Identif. 4 (2020) 452–460, https://doi.org/10.1109/jrfid.2020.3001043.
[15] N. Vidal, J.M. Lopez-Villegas, J. Romeu, A.S. Barenys, A. Garcia-Miquel, G. Gonzalez-Lopez, L. Jofre, 3D-Printed UHF-RFID tag for embedded applications, IEEE Access 8 (2020) 146640–146647, https://doi.org/10.1109/ACCESS.2020.3015335.
[16] J.A. Byford, M.I.M. Ghazali, S. Karuppuswami, B.L. Wright, P. Chahal, Demonstration of RF and microwave passive circuits through 3-D printing and selective metalization, IEEE Trans. Compon. Packag. Manuf. Technol. 7 (2017) 463–471, https://doi.org/10.1109/TCPMT.2017.2651645.
[17] N. Vidal, J.M. Lopez-Villegas, J.A. Del Alamo, Analysis and optimization of multi-winding toroidal inductors for use in multilayered technologies, IEEE Access 7 (2019) 93537–93544, https://doi.org/10.1109/ACCESS.2019.2928179.
[18] Y. Gu, D. Park, S. Gonya, J. Jendrisak, S. Das, D.R. Hines, Direct-write printed broadband inductors, Addit. Manuf. 30 (2019), 100843, https://doi.org/10.1016/j.addma.2019.100843.
[19] C. Tomassoni, O.A. Peverini, G. Venanzoni, G. Addamo, F. Paonessa, G. Virone, 3D printing of microwave and millimeter-wave filters: additive manufacturing technologies applied in the development of high-performance filters with novel topologies, IEEE Microw. Mag. 21 (2020) 24–45, https://doi.org/10.1109/MMM.2020.2979153.
[20] J.M. Lopez-Villegas, N. Vidal, J. Sieiro, A. Salas, B. Medina, F.M. Ramos, Study of 3-D printed conical inductors for broadband RF applications, IEEE Trans. Microw. Theory Tech. 66 (2018) 3597–3602, https://doi.org/10.1109/TMTT.2018.2845862.
[21] G. Zhang, F. Jiao, S. Liu, L. Zhu, S. Wang, Q. Zhang, J. Yang, Compact single-and dual-band filtering 180° hybrid couplers on circular patch resonator, IEEE Trans. Microw. Theory Tech. 68 (2020) 3675–3685, https://doi.org/10.1109/TMTT.2020.3010249.
[22] K.Y. Park, M.I.M. Ghazali, N. Wiwatcharagoses, P. Chahal, Thick 3D printed RF components: transmission lines and bandpass filters, in: Proc. - Electron. Components Technol. Conf., Institute of Electrical and Electronics Engineers Inc., 2018: pp. 2186–2191. ⟨https://doi.org/10.1109/ECTC.2018.00328⟩.
[23] J.M. Lopez-Villegas, A. Salas, N. Vidal, Modeling of 3-D-printed helical-microstrip transmission lines for RF applications, IEEE Trans. Microw. Theory Tech. 67 (2019) 4914–4921, https://doi.org/10.1109/TMTT.2019.2949312.
[24] N. Arnal, T. Ketterl, Y. Vega, J. Stratton, C. Perkowski, P. Deffenbaugh, K. Church, T. Weller, 3D multi-layer additive manufacturing of a 2.45 GHz RF front end, in: Proceedings of 2015 IEEE MTT-S Int. Microw. Symp. IMS 2015, Institute of Electrical and Electronics Engineers Inc., 2015. ⟨https://doi.org/10.1109/MWSYM.2015.7167154⟩.
[25] B.K. Tehrani, R.A. Bahr, W. Su, B.S. Cook, M.M. Tentzeris, E-band characterization of 3D-printed dielectrics for fully-printed millimeter-wave wireless system packaging, IEEE MTT-S Int. Microw. Symp. Dig. (2017) 1756–1759, https://doi.org/10.1109/MWSYM.2017.8058985.
[26] A. Delage, N. Delhote, S. Verdeyme, B. Bonnet, L. Carpentier, C. Schick, T. Chartier, C. Chaput, Aerosol jet printing of millimeter wave transmission lines on 3D ceramic substrates made by additive manufacturing, IEEE MTT-S Int. Microw. Symp. Dig. 2018 (2018) 1557–1560, https://doi.org/10.1109/MWSYM.2018.8439498.
[27] J. Saucourt, N. Jolly, A. Périgaud, O. Tantot, N. Delhote, S. Bila, S. Verdeyme, Design of 3D printed plastic modular filters, in: Eur. Microw. Week 2016 "Microwaves Everywhere", EuMW 2016 - Conf. Proceedings; 46th Eur. Microw. Conf. EuMC 2016, 2016, pp. 369–372. ⟨https://doi.org/10.1109/EUMC.2016.7824355⟩.
[28] E. Lopez-Oliver, C. Tomassoni, L. Silvestri, M. Bozzi, L. Perregrini, S. Marconi, G. Alaimo, F. Auricchio, 3-D-printed compact bandpass filters based on conical posts, IEEE Trans. Microw. Theory Tech. 69 (2021) 616–628, https://doi.org/10.1109/TMTT.2020.3035168.
[29] J.M. López-Villegas, J. Samitier, C. Cane, P. Losantos, J. Bausells, Improvementof the quality factor of rf integrated inductors by layout optimization, IEEE Trans. Microw. Theory Tech. 48 (2000) 76–83, https://doi.org/10.1109/22.817474.
[30] J. Sieiro, J.M. Lopez-Villegas, J. Cabanillas, J.A. Osorio, J. Samitier, A physical frequency-dependent compact model for RF integrated inductors, IEEE Trans. Microw. Theory Tech. 50 (2002) 384–392, https://doi.org/10.1109/22.981290.
[31] T.A. Winslow, Conical inductors for broadband applications, IEEE Microw. Mag. 6 (2005) 68–72, https://doi.org/10.1109/MMW.2005.1418000.
[32] H. Patel, H. Morales, L. Dunleavy, B. Goodhue, Conical inductor modeling using equivalent circuit technique, in: Proceedings of 2015 IEEE 16th Annu. Wirel. Microw. Technol. Conf. WAMICON 2015, Institute of Electrical and Electronics Engineers Inc., 2015. ⟨https://doi.org/10.1109/WAMICON.2015.7120373⟩.
[33] A. Eshkoli, S. Shapira, Y. Nemirovsky, Lumped circuit model of conical-shaped inductors for broad-bandwidth applications, IEEE Trans. Ind. Electron. 63 (2016) 5087–5090, https://doi.org/10.1109/TIE.2016.2546218.
[34] V.N.R. Vanukuru, Millimeter-wave bandpass filter using high-Q conical inductors and MOM capacitors, in: Proceedings of Dig. Pap. - IEEE Radio Freq. Integr. Circuits Symp., Institute of Electrical and Electronics Engineers Inc., 2016, pp. 39–42. ⟨https://doi.org/10.1109/RFIC.2016.7508245⟩.
[35] C. Roda Neve, M. Detalle, P. Nolmans, Y. Li, J. De Vos, G. Van Der Plas, G. Beyer, E. Beyne, High-density and low-leakage novel embedded 3D MIM capacitor on Si interposer, in: Proceedings of 2016 IEEE Int. 3D Syst. Integr. Conf. 3DIC 2016, Institute of Electrical and Electronics Engineers Inc., 2017. ⟨https://doi.org/10.1109/3DIC.2016.7970024⟩.
[36] Y. Lin, C.S. Tan, Physical and Electrical Characterization of 3D Embedded Capacitor: A High-Density MIM Capacitor Embedded in TSV, in: Proc. - Electron. Components Technol. Conf., Institute of Electrical and Electronics Engineers Inc., 2017, pp. 1956–1961. ⟨https://doi.org/10.1109/ECTC.2017.45⟩.
[37] J. Li, S. Ma, H. Liu, Y. Guan, J. Chen, Y. Jin, W. Wang, L. Hu, S. He, Design, fabrication and characterization of TSV interposer integrated 3D capacitor for SIP applications, in: Proc. - Electron. Components Technol. Conf., Institute of Electrical and Electronics Engineers Inc., 2018: pp. 1974–1980. ⟨https://doi.org/10.1109/ECTC.2018.00296⟩.
[38] D.M. Pozar. Microwave Engineering, fourth ed., Wiley, Hoboken, NJ, 2012. ©2012, n.d. ⟨https://search.library.wisc.edu/catalog/9910153599402121⟩.
[39] PathWave EM Design (EMPro) | Keysight, (n.d.). ⟨https://www.keysight.com/es/en/products/software/pathwave-design-software/pathwave-em-design-software.html⟩ (Accessed 17 May 2021).
[40] A. Salas-Barenys, N. Vidal, J. Sieiro, J.M. López-Villegas, B. Medina-Rodríguez, F. M. Ramos, Full-3D printed electronics process using stereolitography and electroless plating, in: Proceedings of the 2017 32nd Conf. Des. Circuits Integr.

Syst. DCIS 2017 - Proc., Institute of Electrical and Electronics Engineers Inc., 2018: pp. 1–4. 〈https://doi.org/10.1109/DCIS.2017.8311624〉.

[41] PathWave Advanced Design System (ADS) | Keysight, n.d. 〈https://www.keysight.com/es/en/products/software/pathwave-design-software/pathwave-advanced-design-system.html〉 (Accessed 20 May 2021).

[42] DWS Systems | Additive manufacturing, n.d. 〈https://www.dwssystems.com/〉 (Accessed 21 May 2021).

[43] K. Angel, H.H. Tsang, S.S. Bedair, G.L. Smith, N. Lazarus, Selective electroplating of 3D printed parts, Addit. Manuf. 20 (2018) 164–172, https://doi.org/10.1016/j.addma.2018.01.006.